

# Balancing Charging Efficiency and Thermal Safety: A Comparative Analysis of Multistage Constant Current Charging Protocols

Meiyuan Jiao, Jianglong Du, Haihua Xu, Jia-hui Li, Michelle Fu, Wenqi Yang, Weiling Luan,\*  
Cheng Lian,\* and Honglai Liu



Cite This: *Ind. Eng. Chem. Res.* 2024, 63, 10054–10066



Read Online

ACCESS |



Metrics & More

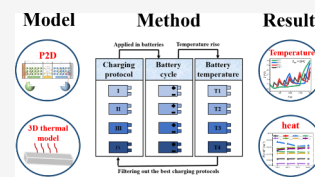


Article Recommendations



Supporting Information

**ABSTRACT:** The fast charging of lithium-ion batteries (LIBs) is crucial for electric vehicle applications yet poses thermal safety challenges. This research delves into the effects of current switching frequency (CSF) within multistage constant current charging (MSCC) protocols on LIBs thermal performance. By integrating electrochemical-thermal model simulations with experimental validation, we reveal that increasing CSF enhances heat dissipation, leading to lower battery temperatures postcharging. Notably, considering the design cost, an 8SCC protocol emerges as the most effective, reducing surface temperatures by approximately 1.5 °C compared to a 2SCC protocol, without compromising charging efficiency. This study provides insights into optimizing MSCC protocols for LIBs, balancing fast charging with thermal stability, which is pivotal for the advancement of high-performance energy storage systems.



## 1. INTRODUCTION

The rapid development of electric vehicles with high energy efficiency and low exhaust emission demands future advanced lithium-ion batteries (LIBs) with high power and energy density and fast-charging capability.<sup>1–4</sup> However, thermal safety limits the development of LIBs.<sup>5–8</sup> Numerous researchers have suggested various alternatives, such as changing the battery electrode structure, altering the battery pack's construction, and improving the heat dissipation mechanism, to increase the thermal safety of LIBs.<sup>9–13</sup> All of these options, however, raise the price of producing LIBs during the manufacturing process. LIBs' thermal safety can be enhanced with low production costs with properly planned charging processes.<sup>7,9–11</sup> Traditional charging protocols advocate applying small currents to the LIBs charging process because large charging currents will increase the battery's heat generation rate. Once the battery temperature exceeds the critical value, the heat control of the battery will fail and the battery may catch fire and explode.<sup>14–16</sup> Therefore, designing and developing new fast-charging protocols that can reduce the heat generation of batteries and improve the performance of batteries are crucial to the development of high energy density and fast-charging LIBs.

As a new fast charging protocol, multistage constant current (MSCC) charging is often employed to reduce the charge time and extend the cycle life of LIBs.<sup>17,18</sup> MSCC charging protocols can reduce the heat generation rate of batteries and enhance the charging performance.<sup>19</sup> Multiple currents that are continuously switched during the charging process consist of the MSCC charging protocol. In addition, the pulse current charging strategy can also improve the charging performance of a lithium-ion battery. Among them, the pulse constant current charging mode (PCCC), by a positive pulsed

current (PPC) followed by a constant current (CC), alternately, can make the battery capacity utilization rate of 80%–95%.<sup>20,21</sup> Inspired by this, this research examines the effect of current switching frequency (CSF) on the thermal behavior of batteries during MSCC charging.

The thermal performance of LIBs has been the subject of numerous experimental studies.<sup>22–24</sup> Currently, the experimental methods adopted to investigate the thermal performance of LIBs are primarily macroscopic in nature. Compared to experimental methods, simulation techniques can efficiently lower the cost by visualizing the processes of ion transport, heat generation, and heat transfer within the LIBs.<sup>25–29</sup> Studies on how fast charging processes affect lithium-ion battery thermal behavior are primarily based on empirical techniques and empirical models, e.g., equivalent circuit models.<sup>26,30</sup> These research techniques fall short of accurately capturing the dynamic behavior of LIBs during the charging process. The pseudo-two-dimensional (P2D) electrochemical model proposed by Newman et al.<sup>31–33</sup> was employed to investigate the dynamic characteristics of LIBs.<sup>31–34</sup> Bae et al. used the electrochemical model to examine the impact of three independent parameters, including the diffusion coefficient of lithium ions, the lithiation rate constant on the surface of the active material, and the particle radius of the active material, on the performance of the batteries.<sup>35</sup> An et al. discovered that the average heat generation rate is relatively unaffected by

Received: March 12, 2024

Revised: May 11, 2024

Accepted: May 14, 2024

Published: May 21, 2024



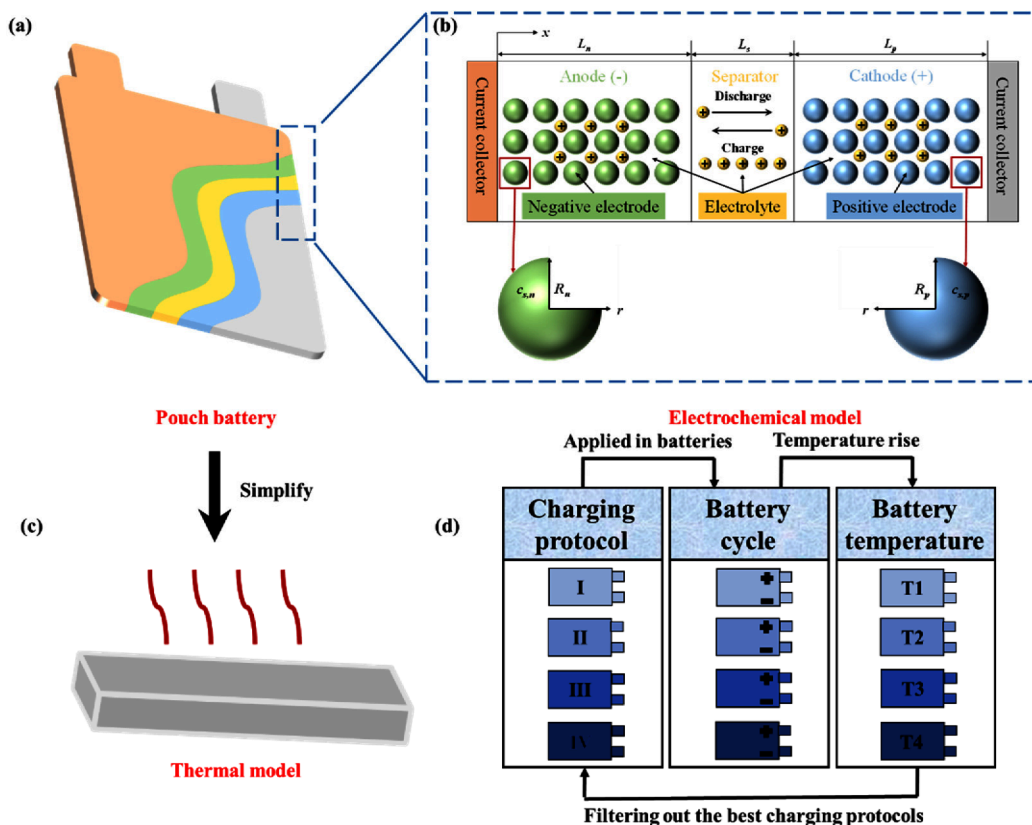


**Figure 1.** (a) Diagram of pouch battery. (b) Electrochemical model diagram. (c) Three-dimensional thermal model schematic. (d) Flowchart of simulation research.

temperature after simulating the thermal behavior and dynamic evolution of electrochemical processes in a battery using an electrochemical model.<sup>36</sup> However, few studies have utilized the electrochemical model to illustrate the influence of the fast-charging protocols on the electrochemical-thermal behavior of batteries.

In this article, a three-dimensional (3D) heat transfer model coupled with a P2D electrochemical model is established to describe the heat generation and transfer processes in the LIBs constructed by  $\text{LiCoO}_2/\text{graphite}$ . We apply different current combinations to the P2D model and calculate the heat generation of LIBs during the charging process. We apply the heat generation calculated by the electrochemical model as a heat source to the three-dimensional thermal model and calculate the temperature of the battery during the charging process. In the fast-charging process, we adopt the charging currents of 1 and 3 C. Combined the designed MSCC charging protocols with different CSFs, we explored the influence of CSF on the battery temperature. The theoretical model is verified by using a commercial  $\text{LiCoO}_2/\text{graphite}$  battery with a 3:7 volume ratio of ethylene carbonate (EC):methyl ethyl carbonate (EMC) electrolyte. Additionally, under various charging protocols, the reversible, joule, and polarization heats in the battery's positive, separator, and negative electrodes are studied. By utilizing multistage constant current charging strategy, the impact of various ambient temperatures on the thermal behavior of the battery is also elucidated.

## 2. MODEL AND METHODS

**2.1. Electrochemical Model.** Figure 1a shows the schematic diagram of a lithium-ion battery, including negative

collector, negative electrode, separator, positive electrode, and positive collector. The numerical simulation for the charging process of a battery, as reported by Newman and Doyle,<sup>31–33</sup> is based on a P2D model as shown in Figure 1b. The P2D model is used to describe the process of ion migration, ion diffusion, and interface reaction in lithium-ion batteries during charging. Therefore, the concentration of lithium ion in the solid and liquid phase is a function of charging time. The control equation in the P2D model is mainly solved by five variables: lithium-ion concentration of the active material particle  $c_s$ , lithium-ion concentration of the electrolyte  $c_e$ , solid potential  $\Phi_s$ , electrolyte potential  $\Phi_e$ , and local current density  $j_r$ .

At the electrode, the governing equation for lithium-ion concentration of the active material particle is

$$\frac{\partial c_s}{\partial t} = \frac{D_s^{\text{eff}}}{r^2} \frac{\partial}{\partial r} \left( r^2 \frac{\partial c_s}{\partial r} \right) \quad (1)$$

where  $r$  is the coordinate along the particle radius direction and  $D_s^{\text{eff}}$  is the effective diffusion coefficient of lithium ions in the active material.

The boundary conditions of the active material particle are

$$\left. \frac{\partial c_s}{\partial r} \right|_{r=0} = 0 \quad (2)$$

$$\left. \frac{\partial c_s}{\partial r} \right|_{r=r_p} = -\frac{j_v}{a_v F} \quad (3)$$

where  $r_p$  is the radius of active particles,  $a_v$  is the specific surface area of active particles, and  $F$  is the Faraday constant.

The governing equation for lithium-ion concentration of the electrolyte is

$$\varepsilon_e \frac{\partial c_e}{\partial t} = D_e^{\text{eff}} \frac{\partial^2 c_e}{\partial x^2} + \frac{1 - t_+^0}{F} j_v \quad (4)$$

where  $\varepsilon_e$  is the volume fraction of the liquid phase,  $c_e$  is the concentration of lithium ions in the liquid phase,  $D_e^{\text{eff}}$  is the effective diffusion coefficient in the electrolyte, and  $t_+^0$  is the transport number.

The boundary condition at the collector is

$$\left. \frac{\partial c_e}{\partial x} \right|_{x=0} = \left. \frac{\partial c_e}{\partial x} \right|_{x=L} = 0$$

$$L = L_{\text{neg}} + L_{\text{sep}} + L_{\text{pos}} \quad (5)$$

The potential of the solid phase is expressed as

$$\sigma^{\text{eff}} \frac{\partial^2 \phi_s}{\partial x^2} = j_v \quad (6)$$

where  $\sigma^{\text{eff}}$  is effective conductivity of the electrode active material,  $\Phi_s$  is the potential in the solid phase, and  $x$  is the coordinate along the battery thickness.

The governing equation for the potential of electrolyte is

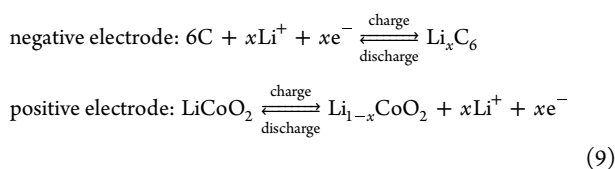
$$k^{\text{eff}} \frac{\partial^2 \phi_e}{\partial x^2} + \frac{\partial}{\partial x} \left( \frac{k^{\text{eff}} 2RT}{F} \right) \left( 1 + \frac{\partial \ln f_{\pm}}{\partial \ln c_e} \right) (1 - t_+^0) \frac{\partial \ln c_e}{\partial x} + j_v = 0 \quad (7)$$

where  $k^{\text{eff}}$  effective conductivity of the liquid phase,  $\Phi_e$  is the potential of the liquid phase,  $R$  is the ideal gas constants, and  $f_{\pm}$  is the mean molar activity coefficient.

No liquid phase current is considered to pass at the boundary of the battery.

$$\left. \frac{\partial \phi_e}{\partial x} \right|_{x=0} = \left. \frac{\partial \phi_e}{\partial x} \right|_{x=L} = 0 \quad (8)$$

During the work process of the lithium-ion battery, the interface reaction occurring on in negative electrode and positive electrode can be described by



The Butler–Volmer equation for interface reaction is described as

$$j_v = a_s i_0 \left[ \exp\left(\frac{\alpha_a F \eta}{RT}\right) - \exp\left(-\frac{\alpha_c F \eta}{RT}\right) \right] \quad (10)$$

where  $a_s$  is the specific surface area of the active particles,  $i_0$  is the exchange current density,  $\eta$  is the overpotential, and  $\alpha_a$  and  $\alpha_c$  are charge transfer coefficients for oxidation and reduction, respectively, assumed to be equal to 0.5.

The exchange current density is calculated by lithium concentration in solid and liquid phases:

$$i_0 = Fk(c_{s,\text{max}} - c_s)^{\alpha_a} (c_s)^{\alpha_c} \left( \frac{c_e}{c_{e,\text{ref}}} \right) \quad (11)$$

where  $k$  is the reaction rate,  $c_{s,\text{max}}$  is the maximum concentration of lithium in the solid phase, and  $c_{e,\text{ref}}$  is the reference concentration in the liquid phase.

The overpotential can be calculated as follows:

$$\eta = \phi_s - \phi_e - E_{\text{eq}} \quad (12)$$

where  $E_{\text{eq}}$  is the equilibrium potential.

Gu and Wang's formulas are used to simulate the heating in accordance with the Rao and Newman's local heating model.<sup>37</sup> The heat produced by two electrodes and separators is included in the battery unit's total heat generation. The heat produced by the collector can be disregarded because of the material's high conductivity. According to the heating method used during charging and discharging, the battery is separated into three heat sources: reaction heat  $Q_{\text{rea}}$ , active polarization heat  $Q_{\text{pol}}$ , and ohmic heat  $Q_{\text{ohm}}$ . The total heat generation  $Q_{\text{total}}$  can therefore be described as

$$Q_{\text{total}} = Q_{\text{rea}} + Q_{\text{pol}} + Q_{\text{ohm}} \quad (13)$$

The reaction heat is mainly caused by reversible electrochemical reactions, so only the reversible heat generated by the positive and negative electrodes is considered and calculated according to the following formula:

$$Q_{\text{rea}} = j_v T \frac{\partial E_{\text{eq}}}{\partial T} \quad (14)$$

The heat of polarization is mainly due to the polarization at the electrochemical interface, and therefore the heat generation in this part of the separator is not considered and can be calculated from the following equation:

$$Q_{\text{pol}} = j_v \eta \quad (15)$$

Ohmic heat is mainly due to the resistance of the active material, the ion migration resistance, and the diffusion resistance in the electrolyte phase, calculated as follows:

$$Q_{\text{ohm}} = \sigma_{s,i}^{\text{eff}} \left( \frac{\partial \phi}{\partial x} \right)^2 + k_{e,i}^{\text{eff}} \left( \frac{\partial \phi}{\partial x} \right)^2 + \frac{2k_{e,i}^{\text{eff}} RT (1 - t_+^0)}{F} \times \left( 1 + \frac{\partial \ln f_{\pm}}{\partial \ln c_e} \right) \frac{\partial \ln c_e}{\partial x} \frac{\partial \phi}{\partial x} \quad (16)$$

**2.2. Three-Dimensional Thermal Model.** In order to describe the heat transfer inside the lithium-ion battery and the heat exchange with the outside, a three-dimensional thermal model has been constructed, as shown in Figure 1c. In the thermal model, the physical properties of the battery are considered to be isotropic, so that the heat conservation equation can be described as

$$\rho C_p \frac{\partial T}{\partial t} + \rho C_p u \nabla T + \nabla(-k_{\text{bat}} \nabla T) = Q_{\text{total}} \quad (17)$$

where  $\rho$  is the battery density,  $C_p$  is the constant pressure heat capacity,  $u$  is the heat flow rate, and  $k_{\text{bat}}$  is the thermal conductivity of the battery.

The boundary conditions of the thermal model are set to heat exchange with the environment.

$$-n(-k_{\text{bat}} \nabla T) = h(T_{\text{ext}} - T) \quad (18)$$

The parameters in the model include constant parameters and temperature/concentration related parameters, which are derived from the literature and estimated.<sup>35,38–40</sup> All

Table 1. 32 min/0–80% SOC Fast Charging Current Protocols

charging protocol	SOC 0% to 10%	SOC 10% to 20%	SOC 20% to 30%	SOC 30% to 40%	SOC 40% to 50%	SOC 50% to 60%	SOC 60% to 70%	SOC 70% to 80%
two-stage CC	1C	1C	1C	1C	3C	3C	3C	3C
four-stage CC	1C	1C	3C	3C	1C	1C	3C	3C
eight-stage CC	1C	3C	1C	3C	1C	3C	1C	3C
sixteen-stage CC	1C 3C	1C 3C	1C 3C	1C 3C	1C 3C	1C 3C	1C 3C	1C 3C

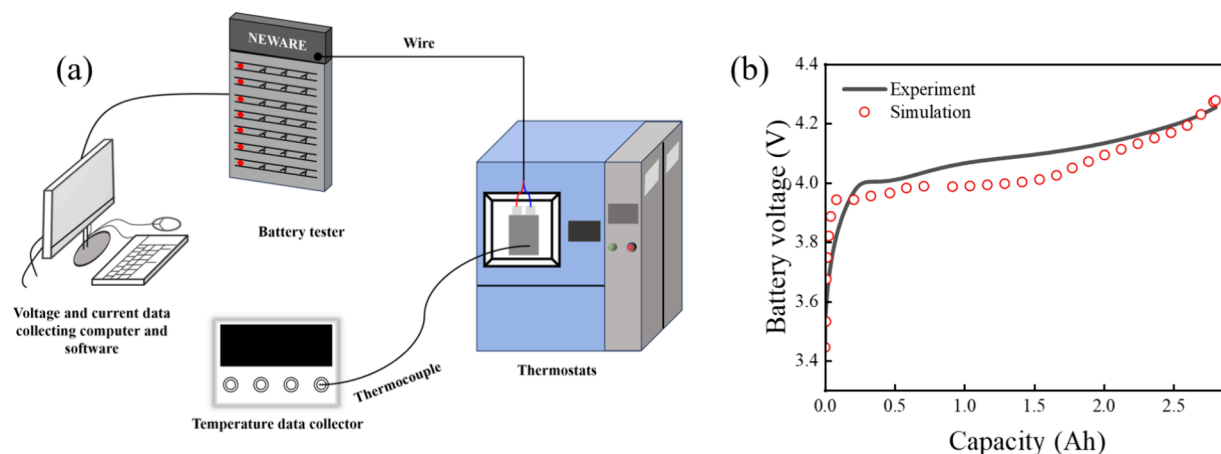


Figure 2. (a) Diagrammatic sketch of the experimental system. (b) Simulation and experiment capacity–voltage curves during charging at a 3C rate.

parameters used in the model are summarized in the [Supporting Information](#).

**2.3. Setting of MSCC Charging Protocol.** We investigate the effect of the CSF on the thermal behavior of the battery with MSCC charging protocol using the electrochemical and thermal models described above and the coupled model built with the commercial software COMSOL Multiphysics. We set up four charging protocols with the same characteristics in order to guarantee the same charging time for various charging procedures: the battery charges to 80% of its rated capacity (80% SOC) in 32 min. [Table 1](#) lists the four charging protocols used in this study. In this table, the 16SCC charging protocol is defined as a multistage constant current charging protocol with 1C and 3C in turn, and the constant current charging depth of each charging stage is 5% SOC. A preferable charging protocol is thought to be the one that results in the battery with a lower temperature rise after charging. The entire simulation study is shown in [Figure 1d](#).

**2.4. Experimental Equipment and Operation.** Commercial  $\text{LiCoO}_2/\text{graphite}$  batteries are applied for experimental testing. The experimental devices are listed in [Figure 2a](#). The test system consists of five parts: a computer with special control software, the Neware battery test system, a constant temperature test chamber (BTT-150D, Guangdong Bell Test Equipment Co., Ltd.), a commercial  $\text{LiCoO}_2$  battery with five thermocouples, and a temperature data collection unit. The Neware battery test system (maximum operating current: 20 A; maximum operating voltage: 20 V) charges the battery and records the current and voltage data, controlled by special software on the computer. The constant temperature test chamber (temperature control range:  $-40$  to  $150$  °C; humidity control range: 10% RH to 98% RH) provides a constant ambient temperature and humidity for the test sample. Five thermocouples are placed evenly on the surface of the battery to measure the temperature of the surface. The temperature

data of the thermocouples are recorded by the temperature data acquisition unit (temperature range:  $-200$  to  $1600$  °C; temperature accuracy:  $0.01$  °C; thermal response time: 1 s) and recorded on the computer.

As it is not easy to accurately measure the SOC of the battery in real time on the experimental equipment, we use different charging currents for different time periods to implement our proposed charging protocol. 2SCC charging protocol: 1C charging current applied for 24 min, 3C charging current applied for 8 min; 4SCC charging protocol: 1C charging current applied for 12 min, 3C charging current applied for 4 min, then repeated once; 8SCC charging protocol: 1C rate charging current applied for 6 min, 3C charging current applied for 2 min, then repeated 3 times. During charging, the thermocouple records five temperatures on the surface of the battery, which are averaged to obtain the average temperature on the surface of the battery and compared to the simulated data. Because of the higher experimental design costs associated with 16SCC, the experimental section only focuses on the first three charging protocols. Subsequent simulations were conducted for the 16SCC protocol to investigate whether adopting an excessively high switching frequency is necessary.

### 3. RESULTS AND DISCUSSION

**3.1. Model Validation.** The validity of the numerical model is verified by comparing it to experimental data. [Figure 2b](#) illustrates the voltage versus charge capacity of the battery at a 3C charge rate. The charging curve demonstrates that the maximum relative error is about 2% between the simulated results and experimental data. In addition, the charging results show a rapid increase in the voltage of the battery at the beginning of the charge, which is due to polarization caused by the charging current applied to the battery. The simulated battery voltage is slightly lower than the experimental battery

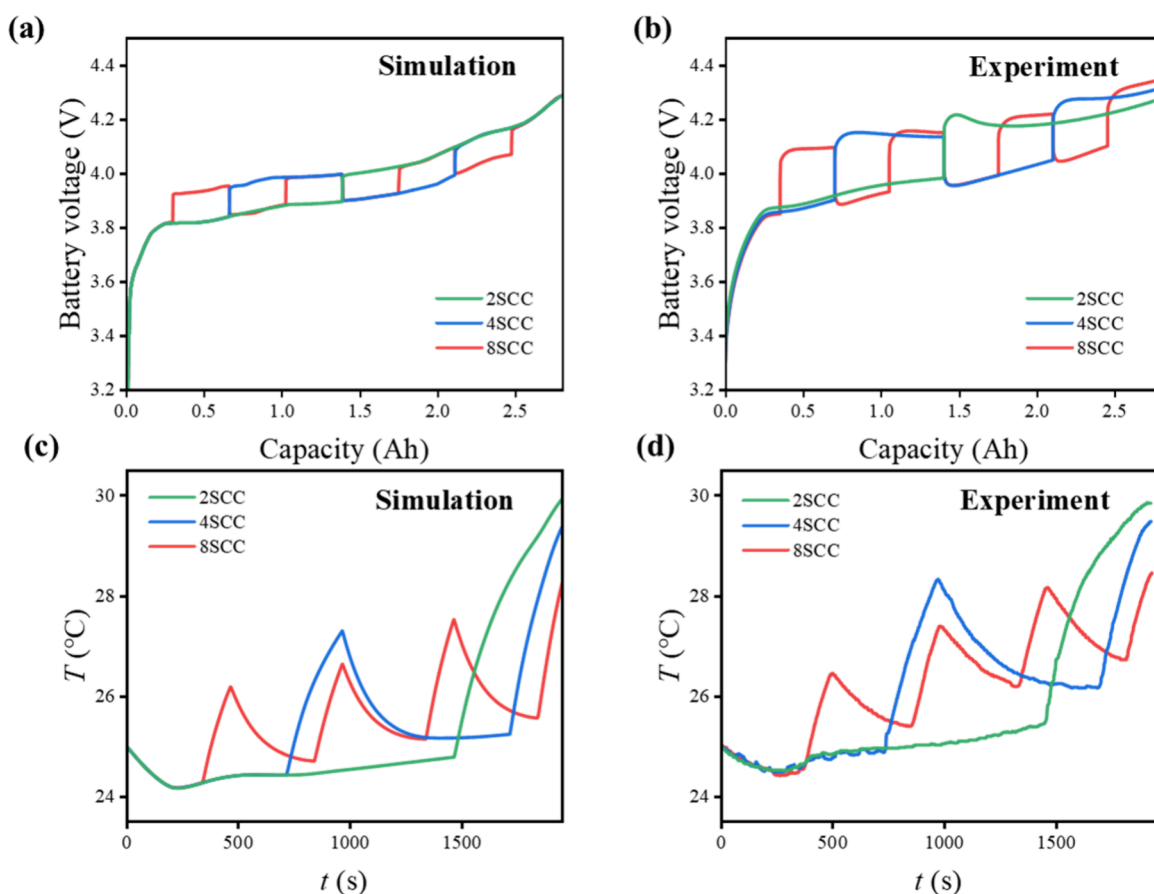


**Figure 3.** (a) Simulated and (b) experimental charging voltage curves with different charging protocols. (c) Simulated and (d) experimental battery temperature curves with different charging protocols.

voltage, which can be attributed to battery polarization. The polarization of the battery includes ohmic polarization caused by the electrode material, electrolyte, separator resistance, and contact resistance of the parts, electrochemical polarization due to the rate of electrochemical reaction on the positive and negative electrodes being less than the speed of electron movement, and concentration polarization due to the diffusion of the lithium ions involved in the reaction in the solid phase being less than the rate of electrochemical reaction. The separator resistance and the contact resistance of the parts are neglected in the present model, which leads to the simulated battery voltage being slightly lower than the experimental value at the beginning of charging. The effect of polarization on the battery voltage becomes less and less as charging proceeds, and the experimental and simulated battery voltages are close.

**3.2. Effect of CSF on Battery Temperature.** Figures 3a and 3b show the voltage changes of the battery during charging at 298 K for simulated and experimental batteries by using different charging protocols. As charging proceeds the battery voltage rises, and when the battery charging current is switched to high current the battery voltage shows a rapid rise; this is because the high current causes an increase in the polarization. Conversely, when the battery charge current is switched to a low current, the battery voltage decreases. The experimental and simulated charging curves show the same trend, which further validates our model.

Figure 3c shows the simulated temperature of the battery surface during charging, where the ambient temperature is 298 K. At the start of charging, there is a drop-in battery

temperature for all three charging protocols due to the fact that the battery is in a state of heat absorption at the start of charging. Apart from the initial drop, the temperature of the battery using the 2SCC charging protocol stays continuously rising, with a sharp increase when the current switches from 1C to 3C. This is caused by the high heat generation of the battery using the high charging current. Once the current reaches 3C, the rate of increase in battery temperature decreases. This is because the rise in the battery temperature will result in an increase in heat exchange between the battery and the external environment, as shown in eq 18. For a lithium-ion battery with 4SCC charging protocol, the surface temperature rises rapidly to a peak after the initial drop; then the charging current drops and so does the battery temperature, before the battery temperature finally rises to a maximum. The final temperature of the battery with 4SCC charging protocol is lower than the temperature of the battery with 2SCC charging protocol. The surface temperature of the battery with the 8SCC charging protocol also varies with the charging current: as the charging current increases, the battery temperature increases; as the charging current decreases, the battery temperature decreases. The final temperatures of the batteries with the three charging protocols from highest to lowest are the batteries with a 2SCC charging protocol, 4SCC, and 8SCC. This suggests that increasing the CSF can be effective in reducing the temperature rise of the battery. Figure 3d shows the experimental rise of the battery, which have the same results as the simulation.

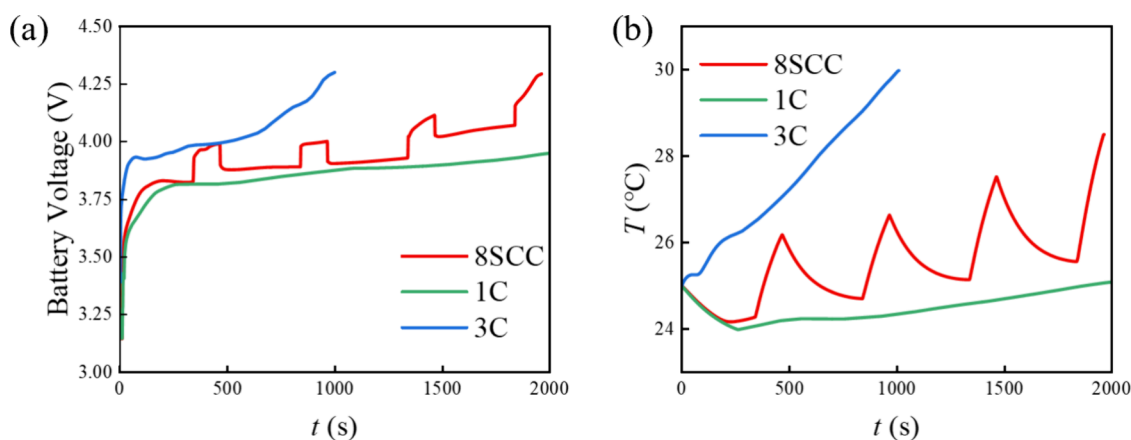


Figure 4. (a) Charge curve and (b) temperature rise of the battery based on a single current and 8SCC charging protocol.

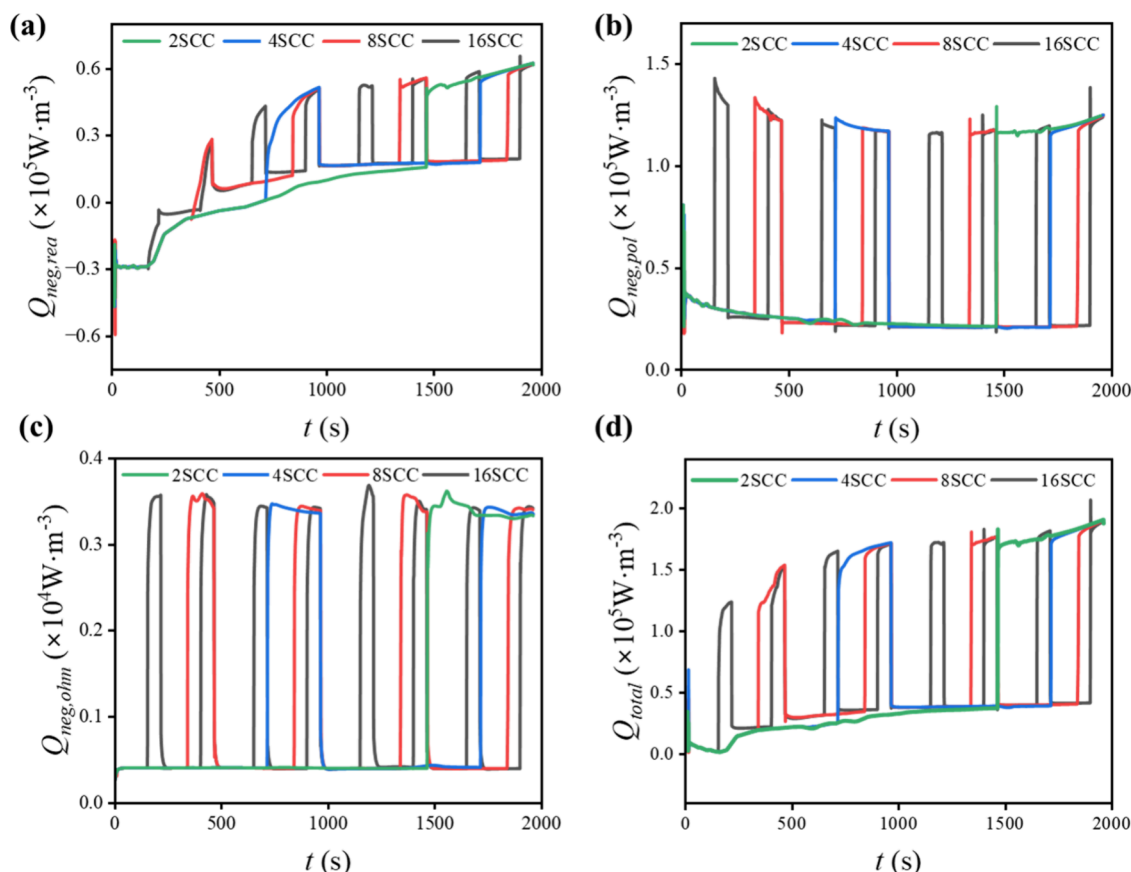
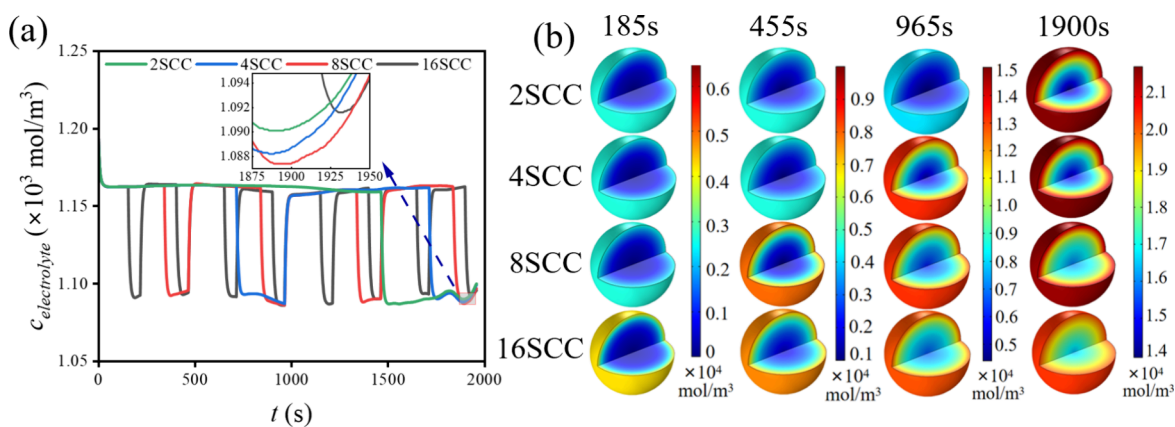


Figure 5. Heat generation rate in the negative electrode: (a) reaction heat generation rate; (b) polarization heat generation rate; (c) ohmic heat generation rate; (d) total heat generation rate.

In the design of the multistage constant current charging protocol, 1C and 3C currents are selected for investigation. Based on this, the final temperature increase of the battery under different current switching frequencies is compared. As illustrated in Figure 3, the accuracy of the simulation is validated. Here, we simulate the voltage change and temperature rise of the battery charged with only 1C and 3C, respectively, as the original comparison sample. According to Figure 4a, it is evident that the battery charged with 3C current has reached 80% SOC at 1000 s and can be charged rapidly. However, the temperature of the battery rises rapidly, reaching a final temperature of 30 °C, as demonstrated in Figure 4b.

When charging with 3C current, there is no significant temperature drop at the beginning, which may be because 3C charging is faster, and the heat absorption stage is shorter. Concurrently, Figure 4 also reflects that the temperature rise of the battery charged only at 1C is slow and the final temperature is also lower, but its charging process is very slow. Meanwhile, the simulation results of the 8SCC charging protocol with the lowest temperature increase are added for comparison. It can be seen that the charging efficiency and charging temperature increase of 8SCC are between the two single-stage constant-current charging protocols. Therefore,



**Figure 6.** (a) Anode electrolyte concentration under four charging protocols. (b) Anode solid-phase lithium ions concentration distribution at 185, 455, 965, and 1900 s.

the single-stage constant-current charging mode is not recommended.

Because of the high design cost of 16SCC, the effect of 16SCC on the cell temperature rise is not studied in the experimental design. By comparison with the experimental results, the validity of the simulation outcomes has been demonstrated. Therefore, subsequent simulations will continue to utilize the constructed model and incorporate the 16SCC charging protocol. We investigate the heat generation rates of the negative electrode, positive electrode, and separator of the battery under four charging protocols to explore the impact of the CSF of multistage constant current on battery temperature. Figure 5 shows the heat of reaction, reversible heat, and joule heat of the negative electrode of the battery during charging.

The reaction heat generation rate for the negative electrode ( $Q_{\text{neg,rea}}$ ) nearly reached  $60 \text{ kW m}^{-3}$  at the end of the charging process as shown in Figure 5a. At the initial period,  $Q_{\text{neg,rea}}$  is negative, which means that the reaction at the negative electrode is heat absorbing at this stage. This is because the temperature equilibrium potential of graphite is positive when its SOC is small, while the local current density in the negative electrode behaves negatively during the charging process, and the heat generation rate of the reaction heat in the negative electrode is calculated to be negative according to eq 14. As the charging proceeds, the thermal behavior on the negative electrode changes from heat absorption to heat release. In the initial stage, the heat generation of the battery is the same for all four charging protocols used.  $Q_{\text{neg,rea}}$  rises when the charging current is switched to a high current. However,  $Q_{\text{neg,rea}}$  did not increase to three times the original one when the charging current was changed from 1C to 3C because it is related to both the temperature equilibrium potential of the electrode material and the charging current.

Figure 5b demonstrates the polarization heat of the negative electrode ( $Q_{\text{neg,pol}}$ ).  $Q_{\text{neg,pol}}$  increases rapidly when the charging current is switched from 1C to 3C. At the end of charging,  $Q_{\text{neg,pol}}$  reaches  $120 \text{ kW m}^{-3}$  for all four charging protocols. Figure 5c shows the ohmic heat of the negative electrode ( $Q_{\text{neg,ohm}}$ ) for the three charging protocols. At the same charging current,  $Q_{\text{neg,ohm}}$  is close at different stages. At a 1C charging current,  $Q_{\text{neg,ohm}}$  is approximately  $4 \text{ kW m}^{-3}$ . At a 3C charging current,  $Q_{\text{neg,ohm}}$  is close to  $34 \text{ kW m}^{-3}$ . Figure 5d shows the total heat generation of the negative electrode ( $Q_{\text{neg,total}}$ ). The results show that the negative electrode exhibits heat absorption at the beginning of charging under all four

charging protocols, which is because the reversible heat on the graphite negative electrode exhibits heat absorption at the beginning of charging and the heat generation on the negative electrode exhibits exothermic heat after a brief performance of heat absorption. In addition, it can be found that the polarization heat occupies the dominant position for the negative electrode heat generation, and the polarized heat generation rate accounts for nearly 2/3 of the total heat generation rate.

In addition, we investigated the changes in the electrolyte concentration at the anode of the battery under four charging protocols, as shown in Figure 6a. From the graph, it can be observed that when the charging current increases to 3C, a significant concentration gradient occurs, which can accelerate ion diffusion and enhance reaction rates. The lowest concentration during the 16SCC charging process occurs in the fourth stage of the 3C current, but it still remains higher than the lowest concentrations observed in the 4SCC and 8SCC scenarios. Notably, the concentration gradients obtained during the four 3C charging stages of 8SCC are higher than those in other protocols during the same time intervals. Meanwhile, we studied the distribution of solid-phase lithium ions concentration in the negative electrode at 185, 455, 965, and 1900 s under the four charging protocols, as shown in Figure 6b. As the charging progresses, the concentration of solid-phase lithium ions in the negative electrode steadily increases. At 185 s, the 16SCC switches the charging current to 3C, resulting in a higher solid-phase lithium ion concentration in the negative electrode compared to batteries using 2SCC to 8SCC. At 455 s, both the 16SCC and 8SCC batteries switch their charging current to 3C, causing their negative electrode particle concentrations to surpass those of the 4SCC and 2SCC batteries. At 965 s, the 4SCC battery also switches its charging current to 3C. It can be observed that at 455 and 965 s, the solid-phase concentration distribution in 8SCC and 16SCC batteries is quite similar, but when all four charging protocols switch to 3C at 1900 s, it becomes evident that the 16SCC battery exhibits a lower solid-phase lithium ion concentration distribution. Furthermore, by combining Figure 6b and Figure 5a, we can see that applying a higher current to the battery leads to the formation of larger concentration gradients in the electrode particles, accelerating ion diffusion, promoting surface reactions, and consequently increasing the heat generation rate of the reactions. Therefore, combined with the change of lithium-ion concentration in liquid and

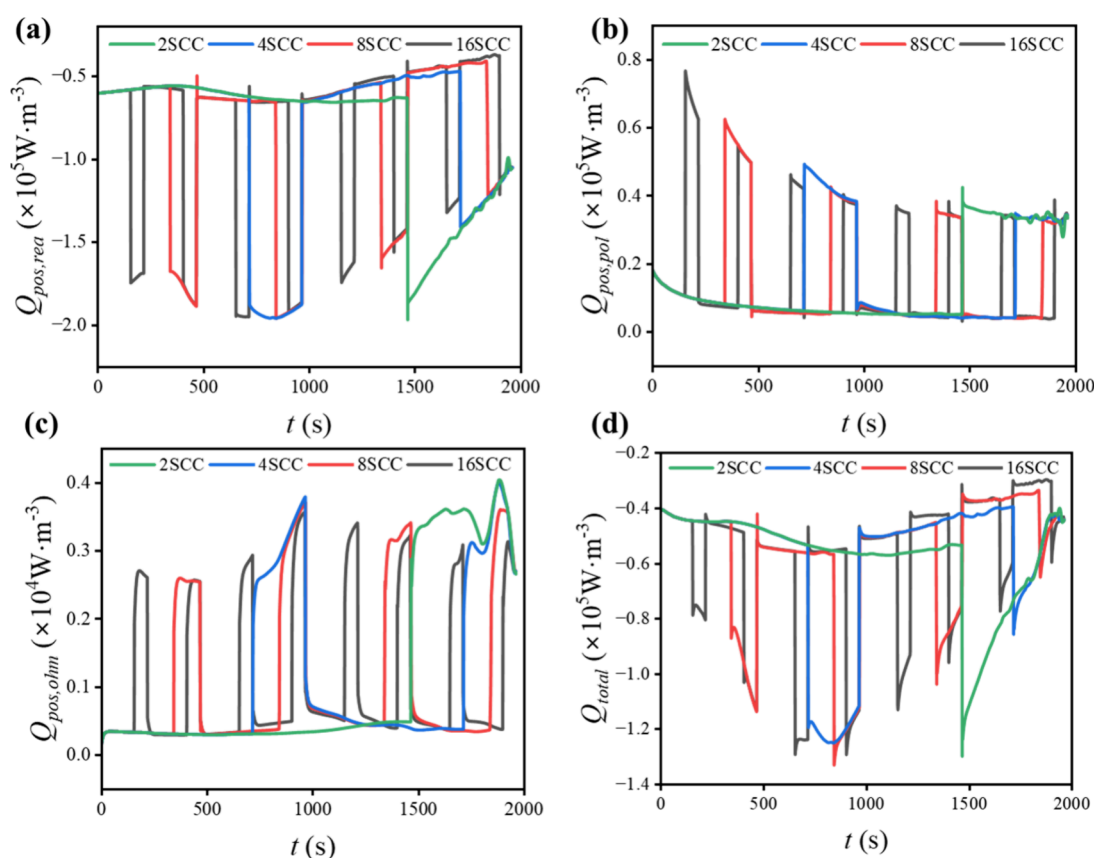


**Figure 7.** Heat generation rate in the positive electrode: (a) reaction heat generation rate; (b) polarization heat generation rate; (c) ohmic heat generation rate; (d) total heat generation rate.

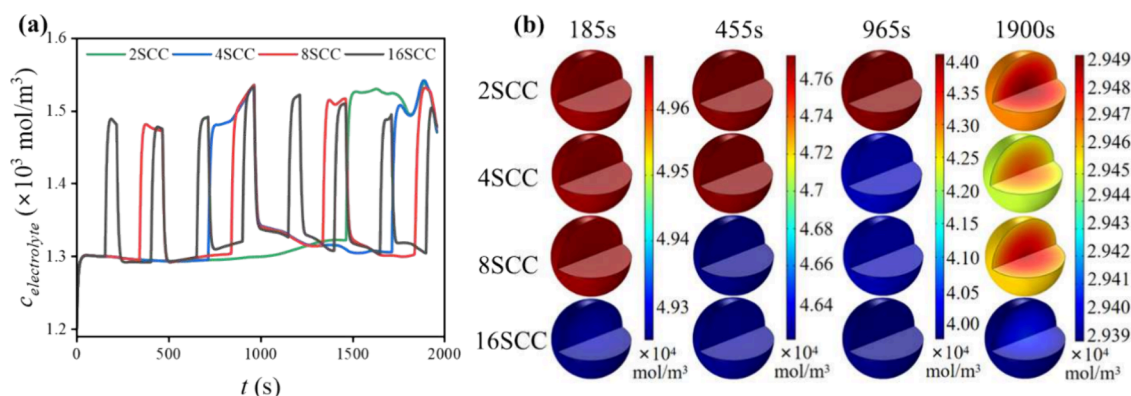


**Figure 8.** (a) Cathode–electrolyte concentration under four charging protocols. (b) Cathode solid-phase lithium ions concentration distribution at 185, 455, 965, and 1900 s.

solid phases, the 8SCC charging protocol has a larger lithium-ion concentration gradient and a higher ion diffusion rate.

Figure 7 shows the heat generation rate in the positive electrode during the charging of lithium-ion batteries using the four charging protocols. Figure 7a shows the reaction heat generation rate ( $Q_{\text{pos,rea}}$ ), and the results show that the positive electrode is in the heat absorption state during the charging process and the heat absorption of the positive electrode increases with the increase of current. Figure 8a displays the electrolyte concentration at the positive electrode, where batteries employing the 8SCC charging protocol exhibit a relatively large concentration gradient during the 3C charging stage. In contrast to the negative electrode, the solid-phase

lithium ion concentration in the positive electrode decreases as the charging progresses; in addition, due to the high concentration of solid lithium ions in the positive electrode, a large concentration gradient is formed in the solid phase, as shown in Figure 8b. Similar to the negative electrode, the charging protocol of 8SCC in the positive electrode is more conducive to ion diffusion.

Figure 7b shows the heat generation rate of polarization heat in the positive electrode ( $Q_{\text{pos,pol}}$ ). The results show that  $Q_{\text{pos,pol}}$  of the battery with the 8SCC charging protocol reaches  $61 \text{ kW m}^{-3}$  when the charging current reaches 3C for the first time, while the highest  $Q_{\text{pos,pol}}$  of the battery with the 2SCC charging protocol reaches  $37 \text{ kW m}^{-3}$ . Figure 7c shows the

ohmic heat generation rate in the positive electrode ( $Q_{\text{pos,ohm}}$ ), and the highest  $Q_{\text{pos,ohm}}$  of the battery using the four charging protocols reaches  $40 \text{ kW m}^{-3}$ . In the positive electrode, the heat generation rate of the reaction heat is greater than the polarization heat and ohmic heat, so the total heat generation of the positive electrode is mainly affected by the reaction heat, as shown in Figure 7d. Therefore, the positive electrode of the battery behaves as heat absorption during charging.

The rate of heat generation in the separator is depicted in Figure 9. The heat generation in the separator considers only

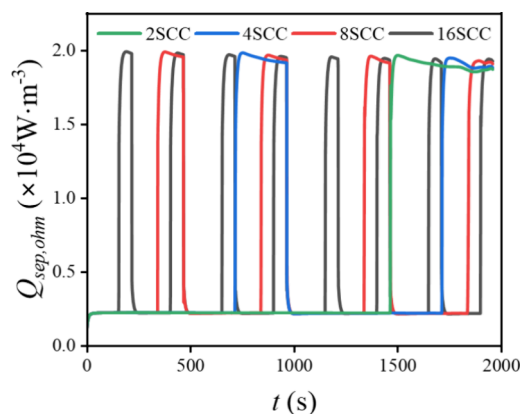


Figure 9. Heat generation rate in the separator.

the ohmic heat in the liquid phase and does not consider the heat of reaction due to interfacial reactions with the polarization heat due to electrochemical polarization at the interface because there is no active material in the separator. The results indicate that the four charging protocols have similar effects on the separator heat generation rates for the cells. The rate of separator heat generation is roughly  $0.22 \text{ kW m}^{-3}$  at a charging current of 1C. The rate of separator heat generation is around  $1.98 \text{ kW m}^{-3}$  at a charging current of 3C. This indicates that the charging current is primarily responsible for the heat generation in the separator, and that the rate of heat generation is proportional to the square of the charging current.

We combine the battery heat generation and calculate the total heat generation of the battery for comparison, as the

graph is unable to show the complete heat generation of the battery under various charging processes.

$$W_i = \int_0^{t_{\text{end}}} Q_i dt \quad (1a)$$

where  $t_{\text{end}}$  is the time when the multistage constant current charging ends.

Figure 10a displays the cumulative heat generation of the battery at different locations at an ambient temperature of  $25 \text{ }^\circ\text{C}$ . The results indicate that as CSF increases, the ohmic heat in the positive electrode decrease, with a turning point observed in the positive electrode reaction heat and negative electrode polarization heat at 8SCC, and the heat generation at other positions increases with the increase of CSF, which leads to the increase of the overall heat generation of the battery with the increase of CSF. This indicates that the battery's heat dissipation, not heat generation, is what accounts for the trend of the final battery temperature of  $2\text{SCC} > 4\text{SCC} > 8\text{SCC} > 16\text{SCC}$  in Figure 10b. Figure S12 shows 3D temperature distributions of the pouch battery with 2SCC, 4SCC, 8SCC, and 16SCC charging protocols at the end of charging with the initial temperature of  $25 \text{ }^\circ\text{C}$ . The results show that the temperature at the center of the battery is greater than the temperature at the surface of the battery, which is due to the heat exchange between the surface of the battery and the environment. At the end of charging for all charging protocols, the maximum temperature difference of the battery is less than  $1 \text{ }^\circ\text{C}$ .

In addition, we supplemented the temperature rise data for batteries using 16SCC and explored the impact of higher CSF on the battery temperature rise, with a decrease in the final battery temperature occurring as the CSF increases, as shown in Figure 10b. It is noteworthy that under the charging protocol with high CSF, the battery temperature drop due to reversible heat will be less in the initial stage, which is because high current will lead to more ohmic heat generation, resulting in increased battery heat generation, and the thermal behavior of the battery will be exothermic, resulting in a temperature rise. In addition, when the current switching times of the MSCC protocol are more than 8 times, the temperature drop of the battery at the end of charging is not obvious. When the current switching frequency of the MSCC protocol exceeds 16 times, the battery's temperature is nearly the same at the end of

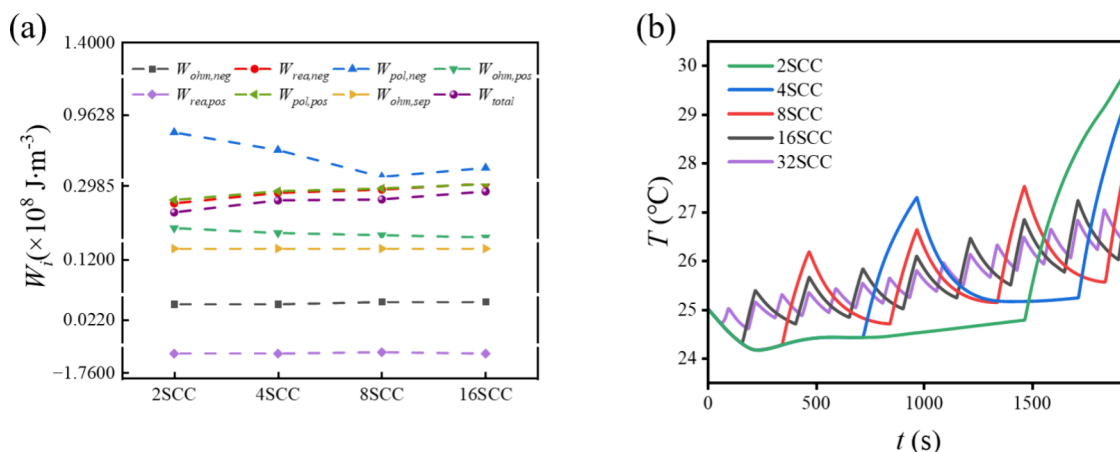


Figure 10. (a) Heat generation in the battery with different charging protocols. (For better viewing, five breakpoints are set in the vertical coordinates in panel (a).) (b) Battery temperature curves with different charging protocols.

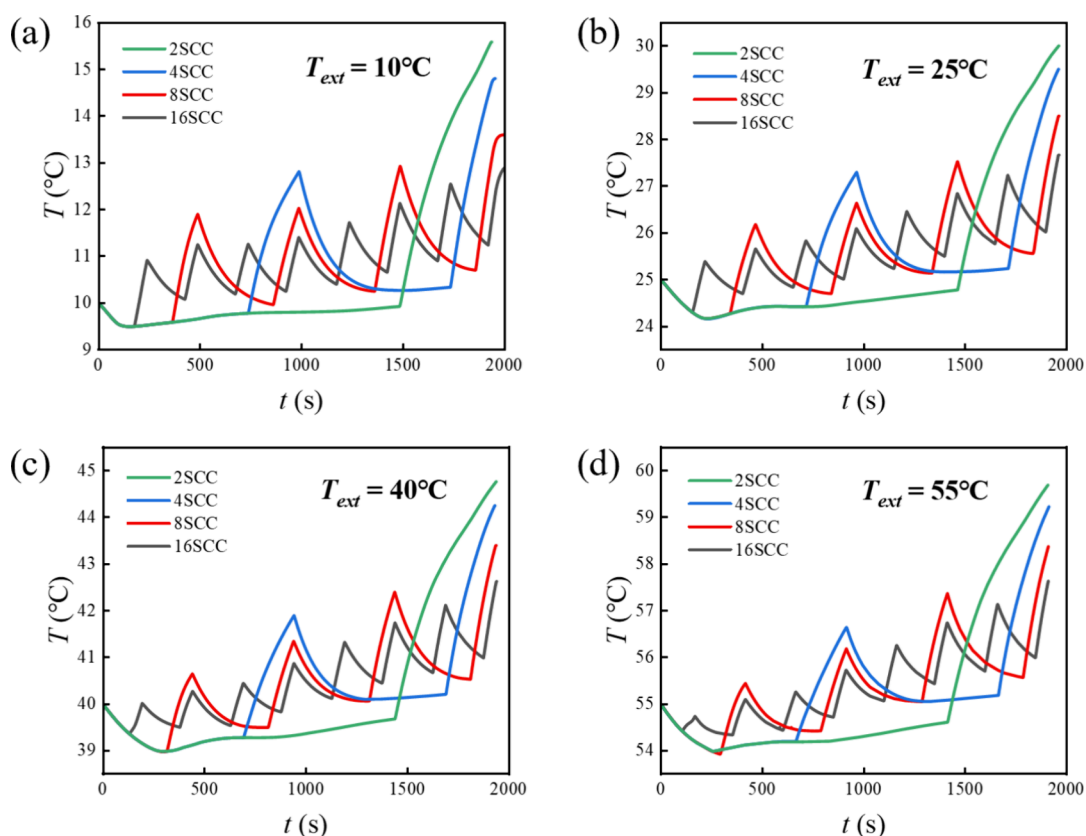


Figure 11. Temperature rise of the battery under different charging protocols at ambient temperatures of (a) 10, (b) 25, (c) 40, and (d) 55 °C.

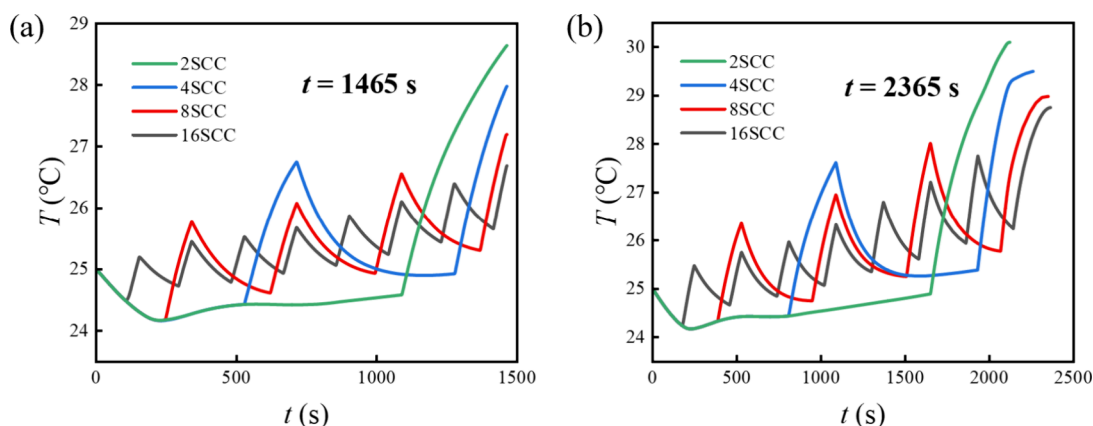


Figure 12. Temperature rise of the battery under different charging protocols: (a) the charge state is 60%; (b) the charge state is 90%.

the charging process. However, the experimental design costs for 16SCC are relatively high, and the electrolyte concentration gradients generated are also lower than those in batteries using 8SCC. Therefore, when there is no strict requirement for battery temperature, it is more advisable to use the 8SCC charging protocol; it is not necessary to pursue too high a switching frequency.

**3.3. Effect of Ambient Temperature on Battery Temperature Rise.** According to eq 18, the ambient temperature is the main factor affecting battery heat dissipation. We simulated the heat generation and temperature rise of batteries using 2SCC, 4SCC, 8SCC, and 16SCC charging protocols at various ambient temperatures in order to more thoroughly study the impact of ambient temperature on battery temperature, as shown in Figure 11. The results

indicate that the battery's temperature rise trend is the same regardless of the ambient temperature, with the battery's temperature rise under the 16SCC charging protocol being the lowest and the battery's temperature rise under the 2SCC charging protocol being the greatest. In addition, as the ambient temperature increases, the initial temperature of the battery rises, which causes the final temperature of the battery to increase using all four charging protocols. As the ambient temperature increases, the final temperature of the battery using the four charging protocols becomes closer to each other because the high ambient temperature weakens the effect of battery heat generation on the battery temperature and brings the battery temperature close to the ambient temperature. The heat generation of the battery at different locations at different temperatures is shown in the Supporting Information.

**3.4. Effect of Total Charge Time on Battery Temperature Rise.** As depicted in Figure 10b, the temperature increase of the battery varies with time during the charging process, ultimately reaching a charged state of 80%, lasting for a total of approximately 2000 s. To further understand whether the order in which the final battery temperature rises is displayed by charging protocols with four different current-switching frequencies varies as the length of charge changes, this study simulates final SOC values of 60% and 90%. As illustrated in Figure 12, the final simulated times are 1465 and 2365 s, respectively. It is evident that regardless of the changes in charging time, the temperature rise pattern of the battery remains consistent, with a higher current switching frequency correlating with a lower final battery temperature. In addition, as the current switching frequency decreases in Figure 12b, the battery SOC quickly reaches 90%, which may be because the battery charge rate slows as the charge state increases. Changing the current from 3C to 1C will greatly reduce the charging rate; 3C charge is used throughout the latter period of the 2SCC charging, thus bringing the SOC of the battery up to 90% earlier.

#### 4. CONCLUSION

A three-dimensional thermal model and a P2D electrochemical model are combined to build a coupling model. Combining simulation and experiment, an MSCC charging protocol is examined to determine the impact of charging CSF on battery temperature rise. The MSCC charging protocols, consisting of a combination of two currents (1C and 3C rate), are designed to “2SCC”, “4SCC”, “8SCC”, and “16SCC”. The battery’s temperature rises rapidly when the charging current is switched from low current to high current. The battery temperature rapidly drops when the charging current is changed to a minimal current. The results indicate that the final temperature of the 2SCC is 30 °C, which is about 1.5 °C higher than that of the 8SCC (28.5 °C). Consequently, by frequently altering the charging current, the temperature increase at high currents remains relatively low, effectively mitigating the escalation of the battery temperature. The research reveals that the polarization heat plays a predominant role in the generation of negative electrode heat, while the positive electrode heat is primarily influenced by the reaction heat. The total heat production of 2SCC is  $2.5 \times 10^7 \text{ J m}^{-3}$ , and that of 8SCC is  $2.74 \times 10^7 \text{ J m}^{-3}$ . By comparing the heat production of the battery under different charging protocols, it is discovered that the order of battery charging protocols from high to low heat production is 16SCC, 8SCC, 4SCC, and 2SCC. The primary reason that the high CSF results in a lower temperature at the end of battery charging is because the high CSF raises the temperature of the battery in multiple stages and enhances the heat exchange between the battery and the ambient temperature. The temperature decrease slows when the charging protocol used exceeds 8SCC, and when it exceeds 16SCC, the final temperature remains nearly the same. Therefore, an excessively high CSF has little impact on lowering the battery temperature rise. We concluded that pursuing a high CSF is not necessary, considering the design expense of the charging protocol. Therefore, 8SCC is the most effective charging protocol. This study fills the gap of current switching frequency in the optimization of multistage constant current charging protocol and facilitates the fast charging of lithium-ion batteries.

#### ■ ASSOCIATED CONTENT

##### Supporting Information

The Supporting Information is available free of charge at <https://pubs.acs.org/doi/10.1021/acs.iecr.4c00971>.

Parameter setting tables for P2D model and 3D thermal model; detailed process diagram of the reaction heat, polarization heat, ohmic heat, and total heat production generated by the battery’s negative, positive, and diaphragm charging under different charging protocols; battery temperature diagram at the end of charging under different charging protocols (PDF)

#### ■ AUTHOR INFORMATION

##### Corresponding Authors

**Cheng Lian** – State Key Laboratory of Chemical Engineering, Shanghai Engineering Research Center of Hierarchical Nanomaterials, School of Chemical Engineering, East China University of Science and Technology, Shanghai 200237, P. R. China; School of Chemistry and Molecular Engineering, East China University of Science and Technology, Shanghai 200237, P. R. China; [orcid.org/0000-0002-9016-832X](https://orcid.org/0000-0002-9016-832X); Email: [lian Cheng@ecust.edu.cn](mailto:lian Cheng@ecust.edu.cn)

**Weiling Luan** – Key Laboratory of Power Battery Systems and Safety (CPCIF), Key Laboratory of Pressure Systems and Safety (MOE), School of Mechanical and Power Engineering, East China University of Science and Technology, Shanghai 200237, P. R. China; Email: [luan@ecust.edu.cn](mailto:luan@ecust.edu.cn)

##### Authors

**Meiyuan Jiao** – State Key Laboratory of Chemical Engineering, Shanghai Engineering Research Center of Hierarchical Nanomaterials, School of Chemical Engineering, East China University of Science and Technology, Shanghai 200237, P. R. China

**Jianglong Du** – School of Chemistry and Molecular Engineering, East China University of Science and Technology, Shanghai 200237, P. R. China

**Haihua Xu** – Key Laboratory of Power Battery Systems and Safety (CPCIF), Key Laboratory of Pressure Systems and Safety (MOE), School of Mechanical and Power Engineering, East China University of Science and Technology, Shanghai 200237, P. R. China

**Jia-hui Li** – School of Chemistry and Molecular Engineering, East China University of Science and Technology, Shanghai 200237, P. R. China; [orcid.org/0000-0002-0985-0525](https://orcid.org/0000-0002-0985-0525)

**Michelle Fu** – Shanghai Qibao Dwight High School, Shanghai 201101, P. R. China

**Wenqi Yang** – State Key Laboratory of Chemical Engineering, Shanghai Engineering Research Center of Hierarchical Nanomaterials, School of Chemical Engineering, East China University of Science and Technology, Shanghai 200237, P. R. China

**Honglai Liu** – State Key Laboratory of Chemical Engineering, Shanghai Engineering Research Center of Hierarchical Nanomaterials, School of Chemical Engineering, East China University of Science and Technology, Shanghai 200237, P. R. China; School of Chemistry and Molecular Engineering, East China University of Science and Technology, Shanghai 200237, P. R. China; [orcid.org/0000-0002-5682-2295](https://orcid.org/0000-0002-5682-2295)

Complete contact information is available at: <https://pubs.acs.org/10.1021/acs.iecr.4c00971>

## Author Contributions

M.J., J.D., and H.X. contributed equally to this work.

## Notes

The authors declare no competing financial interest.

## ACKNOWLEDGMENTS

This work was supported by the National Key Research and Development Program of China (No. 2022YFA1503501), the National Natural Science Foundation of China (No. 22278127, 52375144), the Fundamental Research Funds for the Central Universities (No. 2022ZJFH004), the Shanghai Pilot Program for Basic Research (22T01400100-18), and the Shanghai Rising-Star Program (No. 21QA1401900).

## REFERENCES

- (1) He, Y.-J.; Shen, J.-N.; Shen, J.-F.; Ma, Z.-F. Embedding Monotonicity in the Construction of Polynomial Open-Circuit Voltage Model for Lithium-Ion Batteries: A Semi-infinite Programming Formulation Approach. *Ind. Eng. Chem. Res.* **2015**, *54*, 3167–74.
- (2) Adaykappan, M.; Sathiyamoorthy, N. Modeling, state of charge estimation, and charging of lithium-ion battery in electric vehicle: A review. *Int. J. of Energy. Research.* **2022**, *46*, 2141–65.
- (3) Lai, X.; Chen, Q. W.; Tang, X. P.; Zhou, Y. Q.; Gao, F. R.; Guo, Y.; Bhagat, R.; Zheng, Y. J. Critical review of life cycle assessment of lithium-ion batteries for electric vehicles: A lifespan perspective. *eTransportation* **2022**, *12*, 100169.
- (4) Shafique, M.; Rafiq, M.; Azam, A.; Luo, X. W. Material flow analysis for end-of-life lithium-ion batteries from battery electric vehicles in the USA and China. *Resources Conservation and Recycling* **2022**, *178*, 106061.
- (5) Zhang, X. H.; Li, Z.; Luo, L. A.; Fan, Y. L.; Du, Z. Y. A review on thermal management of lithium-ion batteries for electric vehicles. *Energy* **2022**, *238*, 121652.
- (6) Xu, B.; Lee, J.; Kwon, D.; Kong, L. X.; Pecht, M. Mitigation strategies for Li-ion battery thermal runaway: A review. *Renewable & Sustainable Energy Reviews* **2021**, *150*, 111437.
- (7) Fayaz, H.; Afzal, A.; Samee, A. D. M.; Soudagar, M. E. M.; Akram, N.; Mujtaba, M. A.; Jilte, R. D.; Islam, M. T.; Agbulut, Ü.; Saleel, C. A. Optimization of Thermal and Structural Design in Lithium-Ion Batteries to Obtain Energy Efficient Battery Thermal Management System (BTMS): A Critical Review. *Arch. Computat. Methods. Eng.* **2022**, *29*, 129–94.
- (8) Huang, P.; Tao, H. L.; Yang, J.; Lian, C.; Liu, H. L. Four stages of thermal effect coupled with ion-charge transports during the charging process of porous electrodes. *AICHE. J.* **2022**, *68*, No. e17790.
- (9) Patil, M. S.; Seo, J. H.; Lee, M. Y. A novel dielectric fluid immersion cooling technology for Li-ion battery thermal management. *Energy Conversion and Management* **2021**, *229*, 113715.
- (10) Kong, W.; Zhu, K. J.; Lu, X. P.; Jin, J. T.; Ni, M. Enhancement of lithium-ion battery thermal management with the divergent-shaped channel cold plate. *Journal of Energy Storage* **2021**, *42*, 103027.
- (11) Alihosseini, A.; Shafaei, M. Experimental study and numerical simulation of a Lithium-ion battery thermal management system using a heat pipe. *Journal of Energy Storage* **2021**, *39*, 102616.
- (12) Lin, Y. T.; Lian, C.; Berrueta, M. U.; Liu, H. L.; van Rooij, R. Microscopic Model for Cyclic Voltammetry of Porous Electrodes. *Phys. Rev. Lett.* **2022**, *128*, 206001.
- (13) Lian, C.; Janssen, M.; Liu, H. L.; van Rooij, R. Blessing and Curse: How a Supercapacitor's Large Capacitance Causes its Slow Charging. *Phys. Rev. Lett.* **2020**, *124*, 076001.
- (14) Xie, Y.; Zheng, J. T.; Hu, X. S.; Lin, X. K.; Liu, K. L.; Sun, J. L.; Zhang, Y. J.; Dan, D.; Xi, D.; Feng, F. An improved resistance-based thermal model for prismatic lithium-ion battery charging. *Applied Thermal Engineering* **2020**, *180*, 115794.
- (15) Hasan, M. F.; Chen, C. F.; Shaffer, C. E.; Mukherjee, P. P. Analysis of the Implications of Rapid Charging on Lithium-Ion Battery Performance. *J. Electrochem. Soc.* **2015**, *162*, A1382–95.
- (16) Guo, Z.; Liaw, B. Y.; Qiu, X. P.; Gao, L. L.; Zhang, C. S. Optimal charging method for lithium ion batteries using a universal voltage protocol accommodating aging. *J. Power Sources* **2015**, *274*, 957–964.
- (17) Attia, P. M.; Grover, A.; Jin, N.; Severson, K. A.; Markov, T. M.; Liao, Y. H.; Chen, M. H.; Cheong, B.; Perkins, N.; Yang, Z.; et al. Closed-loop optimization of fast-charging protocols for batteries with machine learning. *Nature* **2020**, *578*, 397–402.
- (18) Zhang, S. S. The effect of the charging protocol on the cycle life of a Li-ion battery. *J. Power Sources* **2006**, *161* (2), 1385–1391.
- (19) Xu, M.; Wang, R.; Reichman, B.; Wang, X. Modeling the effect of two-stage fast charging protocol on thermal behavior and charging energy efficiency of lithium-ion batteries. *Journal of Energy Storage* **2018**, *20*, 298–309.
- (20) Huang, X. R.; Liu, W. J.; Acharya, A. B.; Meng, J. H.; Teodorescu, R.; Stroe, D. I. Effect of Pulsed Current on Charging Performance of Lithium-Ion Batteries. *Ieee Transactions on Industrial Electronics* **2022**, *69* (10), 10144–10153.
- (21) Keil, P.; Jossen, A. Charging protocols for lithium-ion batteries and their impact on cycle life—An experimental study with different 18650 high-power cells. *Journal of Energy Storage* **2016**, *6*, 125–141.
- (22) Liu, X. Y.; Tao, H. C.; Tang, C. Y.; Yang, X. L. Anthracite-derived carbon as superior anode for lithium/potassium-ion batteries. *Chem. Eng. Sci.* **2022**, *248*, 117200.
- (23) Wang, J. T.; Yang, X. J.; Wang, Y. B.; Jin, S. L.; Cai, W. D.; Liu, B. S.; Ma, C.; Liu, X. J.; Qiao, W. M.; Ling, L. C. Rational design and synthesis of sandwich-like reduced graphene oxide/Fe<sub>2</sub>O<sub>3</sub>/N-doped carbon nanosheets as high-performance anode materials for lithium-ion batteries. *Chem. Eng. Sci.* **2021**, *231*, 116271.
- (24) Su, Y.; Chen, S. Q.; Yang, Q. S.; Wang, Y. Self-assembled 3D Fe<sub>2</sub>(MoO<sub>4</sub>)<sub>3</sub> microspheres with amorphous shell as anode of lithium-ion batteries with superior electrochemical performance. *Chem. Eng. Sci.* **2020**, *217*, 115517.
- (25) Sitapure, N.; Lee, H. G.; Ospina-Acevedo, F.; Balbuena, P. B.; Hwang, S.; Kwon, J. S. I. A computational approach to characterize formation of a passivation layer in lithium metal anodes. *AICHE. J.* **2021**, *67*, No. e17073.
- (26) Shen, J. N.; He, Y. J.; Ma, Z. F.; Luo, H. B.; Zhang, Z. F. Online state of charge estimation of lithium-ion batteries: A moving horizon estimation approach. *Chem. Eng. Sci.* **2016**, *154*, 42–53.
- (27) Li, Y. K.; Wei, C.; Sheng, Y. M.; Jiao, F. P.; Wu, K. Swelling Force in Lithium-Ion Power Batteries. *Ind. Eng. Chem. Res.* **2020**, *59* (27), 12313–12318.
- (28) Henquin, E. R.; Aguirre, P. A. Model based analysis of lithium batteries considering particle-size distribution. *AICHE. J.* **2018**, *64*, 904–15.
- (29) Cheng, J.; Tao, H.; Ma, K.; Yang, J.; Lian, C.; Liu, H.; Wu, J. A Theoretical Model for the Charging Dynamics of Associating Ionic Liquids. *Front. Chem. Eng.* **2022**, *4*, 852070.
- (30) Shen, J. N.; He, Y. J.; Ma, Z. F. Simultaneous model selection and parameter estimation for lithium-ion batteries: A sequential MINLP solution approach. *AICHE. J.* **2016**, *62*, 78–89.
- (31) Doyle, M.; Fuller, T. F.; Newman, J. Modeling of Galvanostatic Charge and Discharge of the Lithium/Polymer/Insertion Cell. *J. Electrochem. Soc.* **1993**, *140*, 1526–33.
- (32) Fuller, T. F.; Doyle, M.; Newman, J. Simulation and Optimization of the Dual Lithium Ion Insertion Cell. *J. Electrochem. Soc.* **1994**, *141*, 1–10.
- (33) Doyle, M.; Newman, J.; Gozdz, A. S.; Schmutz, C. N.; Tarascon, J. Comparison of Modeling Predictions with Experimental Data from Plastic Lithium Ion Cells. *J. Electrochem. Soc.* **1996**, *143*, 1890–903.
- (34) Pozzi, A.; Ciaramella, G.; Volkwein, S.; Raimondo, D. M. Optimal Design of Experiments for a Lithium-Ion Cell: Parameters Identification of an Isothermal Single Particle Model with Electrolyte Dynamics. *Ind. Eng. Chem. Res.* **2019**, *58*, 1286–99.

(35) Bae, S.; Song, H.; Nam, I.; Kim, G.-P.; Lee, J.; Yi, J. Quantitative performance analysis of graphite-LiFePO<sub>4</sub> battery working at low temperature. *Chem. Eng. Sci.* **2014**, *118*, 74–82.

(36) An, Z.; Jia, L.; Wei, L.; Dang, C.; Peng, Q. Investigation on lithium-ion battery electrochemical and thermal characteristic based on electrochemical-thermal coupled model. *Applied Thermal Engineering* **2018**, *137*, 792–807.

(37) Gu, W. B.; Wang, C. Y. Thermal-Electrochemical Modeling of Battery Systems. *J. Electrochem. Soc.* **2000**, *147*, 2910.

(38) Allart, D.; Montaru, M.; Gualous, H. Model of Lithium Intercalation into Graphite by Potentiometric Analysis with Equilibrium and Entropy Change Curves of Graphite Electrode. *J. Electrochem. Soc.* **2018**, *165*, A380–7.

(39) Li, J.; Cheng, Y.; Ai, L. H.; Jia, M.; Du, S. L.; Yin, B. H.; Woo, S.; Zhang, H. L. 3D simulation on the internal distributed properties of lithium-ion battery with planar tabbed configuration. *J. Power Sources* **2015**, *293*, 993–1005.

(40) Xu, M.; Zhang, Z.; Wang, X.; Jia, L.; Yang, L. Two-dimensional electrochemical–thermal coupled modeling of cylindrical LiFePO<sub>4</sub> batteries. *J. Power Sources* **2014**, *256*, 233–43.